

# A System for Real-Time XMR Guided Cardiovascular Intervention

Kawal S. Rhode, Maxime Sermesant, David Brogan, Sanjeet Hegde, John Hipwell, Pier Lambiase, Eric Rosenthal, Clifford Bucknall, Shakeel A. Qureshi, Jaswinder S. Gill, Reza Razavi, and Derek L. G. Hill\*

**Abstract**—The hybrid magnetic resonance (MR)/X-ray suite (XMR) is a recently introduced imaging solution that provides new possibilities for guidance of cardiovascular catheterization procedures. We have previously described and validated a technique based on optical tracking to register MR and X-ray images obtained from the sliding table XMR configuration. The aim of our recent work was to extend our technique by providing an improved calibration stage, real-time guidance during cardiovascular catheterization procedures, and further off-line analysis for mapping cardiac electrical data to patient anatomy. Specially designed optical trackers and a dedicated calibration object have resulted in a single calibration step that can be efficiently checked and updated before each procedure. An X-ray distortion model has been implemented that allows for distortion correction for arbitrary c-arm orientations. During procedures, the guidance system provides a real-time combined MR/X-ray image display consisting of live X-ray images with registered recently acquired MR derived anatomy. It is also possible to reconstruct the location of catheters seen during X-ray imaging in the MR derived patient anatomy. We have applied our registration technique to 13 cardiovascular catheterization procedures. Our system has been used for the real-time guidance of ten radiofrequency ablations and one aortic stent implantation. We demonstrate the real-time guidance using two exemplar cases. In a further two cases we show how off-line analysis of registered image data, acquired during electrophysiology study procedures, has been used to map cardiac electrical measurements to patient anatomy for two different types of mapping catheters. The cardiologists that have used the guidance system suggest that real-time XMR guidance could have substantial value in difficult interventional and electrophysiological procedures, potentially reducing procedure time and delivered radiation dose. Also, the ability to map measured electrical data to patient specific anatomy provides improved visualization and a path to investigation of cardiac electromechanical models.

**Index Terms**—Cardiovascular intervention, interventional navigation, XMR systems, 2D-3D registration.

Manuscript received September 13, 2004; revised June 2, 2005. This work was supported in part by the UK-EPSRC under Grant JR/R41019/1, the UK Medical Imaging and Signals IRC, in part by the UK JREI, Philips Medical Systems, and in part by the Charitable Foundation of Guy's & St. Thomas' Hospitals. The Associate Editor responsible for coordinating the review of this paper and recommending its publication was K. Cleary. *Asterisk indicates corresponding author.*

K. S. Rhode, M. Sermesant, D. Brogan, S. Hegde, and R. Razavi are with the Division of Imaging Sciences, Guy's, King's & St. Thomas' School of Medicine, King's College London, Guy's Hospital, London SE1 9RT, U.K.

J. Hipwell is with the Centre for Medical Image Computing, University College London, London WC1E 6BT, U.K.

P. Lambiase, C. Bucknall, and J. S. Gill are with the Department of Cardiology, St. Thomas's Hospital, London SE1 7EH, U.K.

E. Rosenthal and S. A. Qureshi are with the Department of Paediatric Cardiology, Guy's Hospital, London SE1 9RT, U.K.

\*D. L. G. Hill is with the Centre for Medical Image Computing, Malet Place Engineering Building, University College London, Malet Place, London WC1E 6BT, U.K. (e-mail: derek.hill@ieee.org).

Digital Object Identifier 10.1109/TMI.2005.856731

## I. INTRODUCTION

CARDIOVASCULAR catheterization procedures are traditionally carried out under X-ray fluoroscopic guidance. This type of guidance has several advantages for these procedures. The catheters employed are designed to be X-ray visible and can be seen throughout the part of their length that lies in the field of view (FOV) since X-ray imaging is a projection imaging modality. Also, since images can be acquired rapidly [typically, 25 frames per second (fps)], cardiac motion does not cause significant motion artifacts. However, there are some disadvantages that have a significant impact on the catheter guidance and image interpretation. First, since X-ray imaging is a projection imaging modality, more than one view is necessary to gain an appreciation of the three-dimensional (3-D) location and path of catheters. Therefore, there is a need for either moving the X-ray c-arm to obtain different projections or, in a few centers, using a biplane X-ray system for the same purpose. Second, the anatomical context of the acquired images can be difficult to interpret since soft tissues, such as the heart and blood vessels, are not visible during X-ray exposure. Finally, X-ray imaging delivers a radiation dose to the patient and those carrying out the procedure. This can be significant for prolonged procedures and in paediatric cases.

The recent emergence of hybrid X-ray and magnetic resonance (MR) imaging systems (XMR) has opened up new interventional guidance strategies for cardiovascular catheterization procedures. These systems were first proposed as a tool for developing fully MR guided interventions [1], [2]. MR imaging has several advantages over X-ray imaging for guidance. First, MR imaging provides high-quality anatomical information and excellent 3-D visualization of cardiovascular structures. Second, it is also possible to obtain functional information such as cardiac wall motion. Finally, there is no ionising radiation. However, devices that are used during interventions, such as catheters, are not designed to be MR visible or compatible as they often contain ferromagnetic materials or long electrical conductors. Much effort is being directed into making devices MR compatible and visible although the routine use of such devices in patients is still to be established. Many procedures have been successfully carried out using MR guidance in animal models [3], [4] and our group has reported the first clinical use of MR catheter guidance [5].

The aim of our work was to develop an XMR guidance system for cardiovascular interventions that allowed use of both MR and X-ray imaging for guidance. A key step in the development of this system was to register MR and X-ray images that were

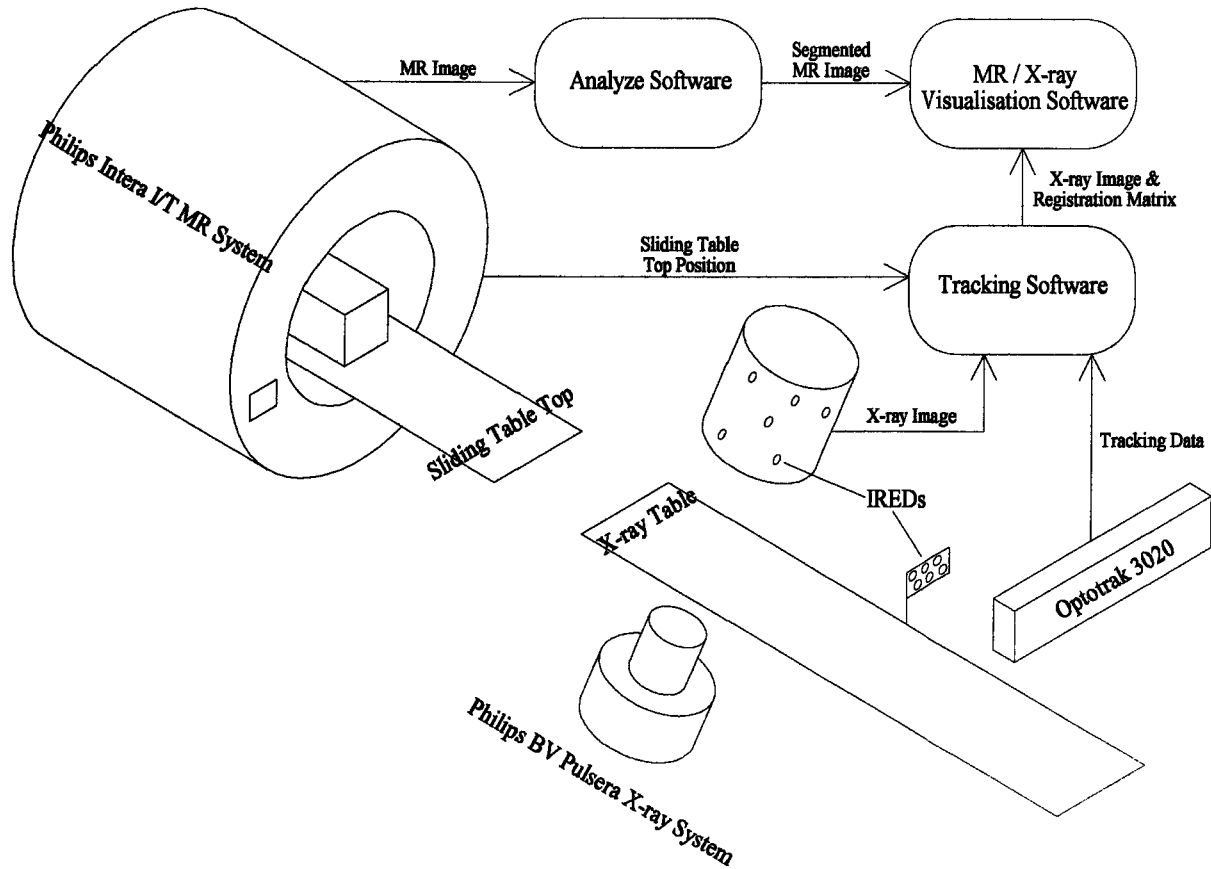


Fig. 1. Schematic showing the components of the XMR guidance system.

acquired of the same patient. We have previously reported and validated such a technique using the sliding table XMR system configuration [6], [7]. This allows the overlay of recently acquired MR derived cardiovascular anatomy onto X-ray images and the reconstruction of the position of catheters seen during X-ray fluoroscopy in this anatomy. Errors in the combined MR and X-ray projection images [two-dimensional target registration error (2D-TRE)] were found to be 2.4–4.2 mm, and the errors in the 3-D reconstruction (3-D TRE) were found to be 4.6–5.1 mm for static phantoms. Our initial system was limited to off-line analysis and required calibration before each patient intervention. We now report on our updated guidance system that provides MR image overlay on real-time X-ray images for guidance during interventions and incorporates X-ray image distortion correction for any c-arm position and an improved single calibration stage.

We have used our guidance system to assist in a total of 13 interventional procedures. All but one of these have been cardiac electrophysiology study (EPS) procedures. EPS procedures are carried out to measure the electrical activity within the chambers of the heart, and may include radiofrequency ablation (RFA) to treat patients that have abnormal heart rhythm by application of radiofrequency energy to ablate the appropriate area of the endocardial surface. EPS procedures are often prolonged and require precise catheter positioning. Therefore, we have focused the use of our guidance system on these procedures. The aim of our on-going program is to augment a variety of EPS procedures by providing a combination of real-time guidance and

off-line analysis. Our system has been used to guide 12 such procedures. The other type of intervention that we have carried out under XMR guidance is the placement of a stent to treat aortic coarctation. This is the first in a series of stenting procedures that are to be performed. We illustrate the real-time use of our guidance system using two exemplar cases, comprising one EPS procedure and the stent placement case. We illustrate the use of our off-line analysis for mapping measured cardiac electrical activity to patient specific MR anatomy for two EPS procedures that used two different types of electrical mapping systems.

## II. METHOD

### A. Description of XMR System

The XMR interventional suite at King's College London (Guy's Hospital Campus) is comprised of a 1.5 T cylindrical bore MR scanner (Philips Intera I/T) and a single plane mobile cardiac X-ray set (Philips BV Pulsera). Patients can be moved in less than 60 s between the two systems using a specially modified sliding table.

### B. Registration and Tracking

1) *Modifications for Registration:* Fig. 1 shows a schematic of the components of the XMR guidance system. MR and X-ray image registration is achieved by a combination of calibration and real-time tracking. The X-ray c-arm and the X-ray table are optically tracked by a Northern Digital Optotrak

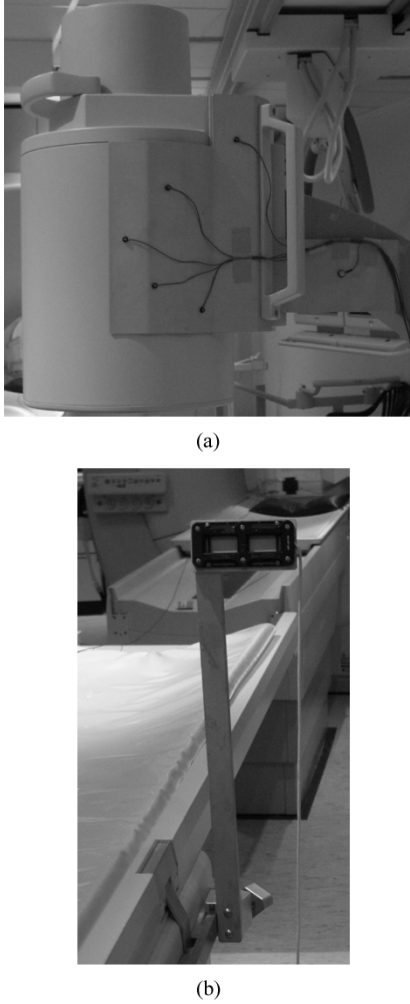


Fig. 2. X-ray c-arm tracker (a) and X-ray table tracker (b).

3020 (NDI, Ontario, Canada) using infrared emitting diodes (IREDs). Tracker objects, each consisting of an array of six IREDs, are affixed to both the c-arm and the X-ray table. The c-arm tracker is an aluminum plate that attaches to the image intensifier and the X-ray table tracker is an aluminum arm that attaches to the X-ray table side rail (Fig. 2). Both these trackers can be removed and reattached in a repeatable manner. This is important for maintaining system calibration. The sliding table is tracked by the MR system software while docked to the MR scanner and becomes part of the X-ray table when docked to the X-ray system and is then tracked by the Optotrak. The guidance software operates on a single workstation and has two components. The first component is the tracking software that performs X-ray image frame capture, system calibration and real-time computation of image registration. The second component is the visualization software that performs the combined display of MR and X-ray images. A further workstation is used for the Analyze software (Mayo Clinic, Rochester, MN). This software allows semi-automatic segmentation of cardiovascular MR images.

2) *Updating Registration During a Procedure:* The registration and tracking described in Section II-B1 assume that the patient does not move with respect to the tracked table during the procedure. This assumption works well for anaesthetized

ventilated patients, where the patient does not move on the table, and the end-expiration position in the respiratory cycle is repeatable. For sedated patients, however, this assumption breaks down both because of nonreproducible breath hold position, and because the patient may not lie still. For cardiovascular interventions in the chest, unlike procedures in the head, it is not possible to directly track the subject with high accuracy in 3-D. Indeed any subject motion is likely to include tissue deformation. Two strategies were employed to deal with possible gross motion of the patient. First, specially designed Velcro straps were placed over the chest to keep the patient as immobile as possible. Second, a single donut shaped skin marker (Multi-modality radiographic marker, IZI Medical Products Corp., Baltimore, MD) was placed just below the sternal notch. This marker is impregnated with gadolinium to make it MR visible. It also had a central hole that can accept a 3-mm steel ball bearing to make it X-ray visible. Although this marker cannot accurately record all motion, it provides an indication of motion and a means for updating registration with a translation. During MR imaging, a multislice end-expiration volume is acquired that includes the marker. The position of the marker in the volume is then found by manual marking. During X-ray imaging, a ball bearing is placed in the central hole of the marker and biplane end-expiration imaging is used to compute the location of the marker in the coordinate system of the MR volume. Since our X-ray system is single plane, the c-arm must be repositioned to achieve the biplane views. The correcting translation can then be computed and used to correct the registration matrix.

### C. Calibration

1) *X-Ray Image Distortion Correction:* X-ray image distortion can be divided into two components. The first component is the pincushion distortion. This results from the mapping of electrons from the curved input screen of the image intensifier to the flat output screen. This component is static and is not affected by the orientation of the image intensifier. The second component is the spiral distortion (S-distortion). This results from the effect of the magnetic field surrounding the image intensifier on the electron trajectory. This component is not static and changes with image intensifier orientation.

X-ray image distortion correction is carried out by computing the transformation that maps points from corrected image space to distorted image space. A corrected image can be formed from the distorted image by applying this transformation together with an interpolation scheme. This method is termed 'global' correction. Polynomial transformations have been used to implement global correction. Third-order polynomials were used by [8]

$$\begin{aligned}
 x' &= f_0 + f_1y + f_2x + f_3y^2 + f_4xy \\
 &\quad + f_5x^2 + f_6y^3 + f_7y^2x + f_8yx^2 + f_9x^3 \\
 y' &= g_0 + g_1y + g_2x + g_3y^2 + g_4xy \\
 &\quad + g_5x^2 + g_6y^3 + g_7y^2x + g_8yx^2 + g_9x^3
 \end{aligned} \quad (1)$$

where  $(x, y)$  is a point in corrected image space,  $(x', y')$  is a point in distorted image space, and  $f_i, g_i$  are the coefficients of the correcting polynomials.

Given a sufficient number of corresponding points in distorted and corrected image spaces, it is possible to compute the coefficients  $f_i, g_i$  by separate least squares minimization of the terms

$$\begin{aligned} S_X &= \sum_i (x_i - x'_i)^2 \\ S_Y &= \sum_i (y_i - y'_i)^2. \end{aligned} \quad (2)$$

It was shown in [9] that using higher order polynomials significantly improves the residual error up to fifth-order but using higher orders than this has no statistical improvement. There are 10 polynomial coefficients for third-order and 21 for fifth-order. Therefore, there is an increase in computational cost by increasing polynomial order but this is offset by the improvement in residual error.

The global scheme allows image correction for a single image intensifier orientation. Methods have been proposed to correct image intensifier distortion for a range of orientations. These schemes can be termed ‘super global.’ In super global correction, each of the correcting polynomial coefficients is expressed as polynomial function of image intensifier angulation. [10] devised a super global scheme that modeled distortion as a function of left-right image intensifier angulation over a range of  $220^\circ$ . [11] extended this approach to include craniocaudal image intensifier angulation.

For our application, the c-arm can be freely moved during an intervention. Therefore, it was required to develop a super global correction scheme that modeled distortion as a function of any image intensifier orientation. The position of the image intensifier is tracked by the guidance software. The obtained tracking matrix can be decomposed to give the translational and rotational components. The translational components are ignored and the rotational components are used for the super global model. Each of the global polynomial coefficients in (1) can be expressed as a polynomial function of the rotational component

$$\begin{aligned} f'_i &= F_{i,0} + F_{i,1}\alpha + F_{i,2}\beta + F_{i,3}\gamma + F_{i,4}\alpha\beta \\ &\quad + F_{i,5}\beta\gamma + F_{i,6}\alpha\gamma + F_{i,7}\alpha^2 + F_{i,8}\beta^2 + F_{i,9}\gamma^2 + \dots \\ g'_i &= G_{i,0} + G_{i,1}\alpha + G_{i,2}\beta + G_{i,3}\gamma + G_{i,4}\alpha\beta \\ &\quad + G_{i,5}\beta\gamma + G_{i,6}\alpha\gamma + G_{i,7}\alpha^2 + G_{i,8}\beta^2 + G_{i,9}\gamma^2 + \dots \end{aligned} \quad (3)$$

where  $(\alpha, \beta, \gamma)$  are the Euler angles derived from the rotational component,  $F_{i,j}, G_{i,j}$  are the super global polynomial coefficients for global coefficients  $f_i, g_i$ , and  $f'_i, g'_i$  are the global coefficients estimated by the super global model. The number of terms in (3) depends on the order of the super global polynomial. Third-order has 20 coefficients and fifth-order has 56. Given a series of images for which the global coefficients and the angles are known, it is possible to find the super global coefficients by separate least squares minimization of the terms

$$\begin{aligned} S_{F_i} &= \sum_j (f_{i,j} - f'_{i,j})^2 \\ S_{G_i} &= \sum_j (g_{i,j} - g'_{i,j})^2. \end{aligned} \quad (4)$$

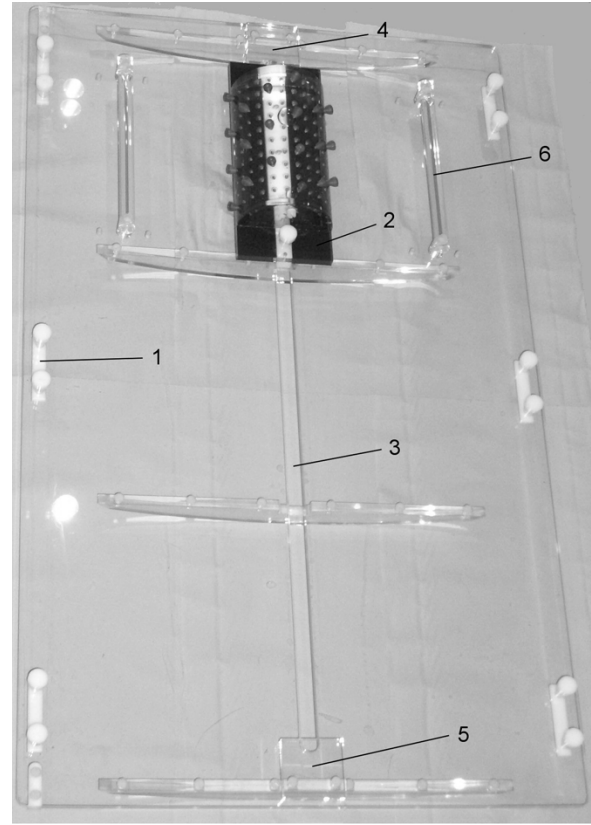


Fig. 3. Calibration object. 1—Fixing flange for sliding table. 2—Saline-filled acrylic half cylinder with 21 divot cap markers in a helical arrangement. 3—Slot in acrylic base plate to allow sliding of half cylinder. 4 and 5—End stops. 6—Fixing to allow MR surface coil attachment.

In order to implement the super global distortion model, we used a 400-mm-diameter ball grid with ball bearings of 1-mm diameter and grid spacing of 15 mm. This was attached to the input surface of the image intensifier casing. We acquired tracked X-ray images of this grid for 26 different c-arm trajectories. In total 4611 grid images were acquired covering the full range of image intensifier orientations that are likely to be encountered during an intervention. For each image the positions of the ball bearings were automatically found and the global distortion parameters were computed using fifth-order polynomials [(1) and (2)]. Using this data, the super global model was formed also using fifth-order polynomials [(3) and (4)]. Now, given any tracked X-ray image acquisition, it was possible to correct the geometric distortion using the super global model. We tested our model by acquiring 35 grid images at different c-arm orientations and comparing the residual root-mean-square (RMS) error using global correction (the gold standard) and using the super global model. For application to images acquired during interventions, the super global distortion model was included in the guidance system software. X-ray images were automatically corrected after acquisition using the model and bilinear interpolation.

2) *Calibration Object Imaging:* Calibration of the system involves imaging a specially designed acrylic calibration object (Fig. 3). This object consists of a half cylinder that can accept 120 interchangeable fiducial markers. These markers are of two types. The first type has a cylindrical cap that can be filled with

a mixture of gadolinium and iodine contrast agents. The second type has a cap with a 3-mm divot on top. This divot can either accept a 3-mm-diameter ball bearing or the tip of an Optotrak pointing device. The fluid-filled cap markers are used during MR imaging and the divot cap markers with ball bearings are used during X-ray imaging of the calibration object. The half cylinder is hollow and is filled with saline to provide loading during MR image acquisition. It is mounted on a base plate that locks onto the sliding table in a fixed position. The half cylinder can slide in the direction of motion of the sliding table between two fixed positions on the base. Although the half cylinder can accept up to 120 markers, 21 markers positioned in a helical arrangement were used to perform calibration for the 23 cm X-ray FOV. This number of markers provided coverage of the X-ray FOV without resulting in superposition of markers in the different X-ray views. The calibration object was imaged using a T1-weighted 3-D GRE MR sequence ( $256 \times 256$  matrix, 200 slices, resolution =  $1.05 \times 1.05 \times 1.2$  mm<sup>3</sup>, TR = 14.0 ms, TE = 6.05 ms, flip angle =  $15^\circ$ , scan time  $\sim 6$  min) with the fluid-filled cap markers in place. The position of the 21 markers was found semi-automatically in the MR volume. The calibration object was then transferred to the X-ray system and the fluid-filled cap markers were changed for the divot cap markers. The position of the markers was determined using the Optotrak pointer in both of the two possible positions of the half cylinder. Ball bearings were inserted into the divots and 39 tracked X-ray views were acquired for a range of c-arm orientations. These images were automatically corrected for geometric distortion using the super global model as described in Section II-C1. A total of 398 ball bearings were visible in the 39 X-ray images. The position of the ball bearings was found automatically in each of the images. These data were then used to compute the positional relationship between the MR scanner and the X-ray system, the perspective projection parameters of the X-ray system, and the translation vector of the sliding table [6]. Once the system was calibrated, it was possible to register any MR image acquisitions to X-ray image acquisitions. Before each intervention, the calibration was checked by carrying out X-ray imaging of the calibration object and visually checking alignment with the projected MR volume of the object. Movement of the tracker objects would invalidate the calibration. However, due to the design of the calibration object, it would be possible to correct this by reacquiring the location of the markers using the Optotrak pointer. This process would only take a few minutes and a complete recalibration, taking several hours, is not necessary.

#### D. Interventional Functionality

1) *Combined MR Anatomy With Live X-ray Image Display:* During interventions the guidance system can provide a recently acquired MR anatomy overlay onto real-time X-ray images. The guidance software runs on a workstation with a dual monitor display. One monitor is used to display the control interface and the second monitor displays the image overlay. First, the patient undergoes MR anatomy imaging. The images are semi-automatically segmented to isolate the anatomy of interest. A surface rendering is produced in VTK format (Kitware Inc., Clifton Park, NY) using the marching cubes algorithm. During

X-ray image acquisition, the tracking software frame captures the X-ray image at 25 fps and then carries out distortion correction. The software also computes the two-dimensional to three-dimensional (2D–3D) registration matrix using the calibration data and the tracking data from the Optotrak. The visualization software uses the registration information to display the anatomical surface in the correct orientation over the X-ray image at 3 fps.

2) *X-Ray View Selection:* One further feature of the guidance system was the ability to carry out X-ray view selection without administration of X-ray dose. In this mode, the tracking software passes the registration data to the visualization software without performing X-ray image capture. As the c-arm is moved without carrying out fluoroscopy, the position of the anatomical surface is updated by the visualization software. Therefore, the radiographer can position the c-arm to give the required view of the anatomy without dose administration to the patient.

3) *Three-Dimensional Catheter Reconstruction:* With biplane X-ray image acquisition, it is possible to use the registration data to reconstruct and display the location of catheters in the MR anatomy. This is performed semi-automatically with the user clicking on points along the catheter in the biplane images [12]. This could be fully automated but the semi-automatic approach takes less than one minute, which is within our current requirement. The X-ray images are acquired at end-expiration and only the end-diastolic images are selected to match the respiratory and cardiac phase of the MR acquisition, respectively.

#### E. Clinical Applications

The system described has wide applicability to endovascular procedures in which X-ray guidance is normally used, but where additional anatomical information would be desirable. In the following sections we describe the methodology used to apply our system to the real-time guidance of procedures and how off-line analysis was used for EPS procedures to map measured cardiac electrical activity to MR anatomy.

The patients investigated all gave informed consent to take part in this research that used a local research ethics committee approved protocol.

1) *Real-Time Guided Procedures:* We used the system for real-time guidance of EPS procedures in 10 patients and during stent implantation for coarctation of aorta in one patient. Nine of the EPS cases were patients with intermittent atrial fibrillation undergoing electrical isolation of pulmonary veins (PVs). The remaining EPS case was a patient undergoing RFA for a focal right ventricular tachycardia. The typical protocol was as follows. The patient was placed on the sliding table and transferred to the X-ray side. All EPS procedures were carried out under local anaesthesia and sedation. The aortic stent placement was carried out under paralysis and general anaesthesia. Sheaths were inserted to gain vascular access. The patient was then transferred over to the MR side. Two MR scans were performed, one was a multislice volume using a 3-D GRE sequence (typically,  $512 \times 512$  matrix, 40 slices, resolution =  $0.68 \times 0.68 \times 1.4$  mm<sup>3</sup>, TR = 4.3 ms, TE = 1.45 ms, flip angle =  $40^\circ$ , scan time  $\sim 20$  s) that included the skin marker, and the other was a gadolinium enhanced MRA scan using a 3-D GRE sequence (typically,  $512 \times 512$  matrix, 50 slices, resolution =  $0.84 \times 0.84 \times 1.8$  mm<sup>3</sup>, TR = 3.8 ms,

TE = 1.2 ms, flip angle = 40°, scan time  $\sim$  20 s) capturing the appropriate anatomy. Both scans were carried out during end-expiration using either breath-hold or ventilator control. The patient was then transferred to the X-ray side and the ball bearing was inserted into the center of the skin marker. The MR scans were transferred to the guidance system workstation. The location of the skin marker was determined in the MR volume and the MRA scan was processed to generate the anatomical surface. For the EPS procedures, the endocardial surface was used. During the procedure, the guidance system displayed the MR derived anatomical surface overlaid onto the X-ray images of the catheters being used. When required, biplane X-ray images were acquired of the catheters during end-expiration and the 3-D location of these catheters was reconstructed and displayed in the MR derived anatomy using the end-diastolic images. The view selection mode of the guidance system (Section II-D2) was also used at times to orientate the c-arm to gain the appropriate X-ray view. Since there was periodic X-ray angiography with iodine contrast, it was possible to notice any misregistration that may have been caused by gross patient motion. When such motion occurred, we were able to apply the translation correction described in Section II-B2.

2) *Mapping Measured Electrical Activity to MR Derived Anatomy*: In two patients undergoing EPS procedures, we were able to project the measured electrical activity on to MR derived anatomy. Two different types of electrical mapping systems were used. For the first patient (patient 1), a multielectrode basket catheter was used (Constellation catheter, Boston Scientific, MA, [www.bostonscientific.com](http://www.bostonscientific.com)) [13]–[15]. For the second patient (patient 2), a noncontact mapping system was used (EnSite, Endocardial Solutions Inc., St. Paul, MN, [www.endocardial.com](http://www.endocardial.com)) [17], [18]. The protocol for these patients was similar to that described in Section II-E1, however, these studies were performed prior to the availability of the real-time overlay visualization. Therefore, the processing of all acquired data was off-line. The initial MR scans of the anatomy were performed using a 3-D multiphase SSFP sequence (typically, five phases,  $256 \times 256$  matrix, 152 slices, resolution =  $1.33 \times 1.33 \times 1.4$  mm<sup>3</sup>, TR = 3.0 ms, TE = 1.4 ms, flip angle = 45°, trigger delay for phase 5 = 383 ms, heart rate = 132 min<sup>-1</sup>, scan time  $\sim$  5 min) during end-expiration. We minimized cardiac motion blurring by making the gating window as small as possible while taking into account the total scan time. Myocardial motion imaging was also performed in both short axis (SA) and long axis (LA) views using a SPAMM tagged imaging sequence (typically, 35 phases,  $256 \times 256$  matrix, nine slices SA and five slices LA, resolution =  $1.76 \times 1.76 \times 12.05$  mm<sup>3</sup>, TR = 13.0 ms, TE = 1.1 ms, flip angle = 30°, tag spacing = 6 mm, scan time  $\sim$  20 s per slice). The patient was then transferred to the X-ray system.

For patient 1, four electrical measurement catheters were inserted into the patient's right ventricle. Three of these were multipolar catheters and the fourth was the Constellation basket catheter. Dynamic biplane tracked X-ray images were acquired with the catheters in place and at the same time the electrical activity was recorded from the Constellation catheter during one normal and one ventricular ectopic beat. The X-ray image acquisition was carried out at end-expiration to match the phase

of ventilation during which the MR images were acquired. For patient 2, three electrical measurement catheters were inserted into the patient's heart. One was a quadrupole catheter that was placed in the right ventricle; one was the EnSite system's balloon catheter that was placed in the left ventricle; and the other was a decapole catheter that acted as the EnSite system's roving catheter that was also placed in the left ventricle. Initially, the roving catheter was moved along the endocardial surface of the left ventricle and the EnSite system tracked its position to generate a surface representation of this chamber. The balloon catheter then measured the electrical activity and the EnSite software extrapolated this to the reconstructed left ventricular surface. Dynamic biplane tracked X-ray images were acquired with the catheters in place. Furthermore, the locations of the four most distal electrodes on the roving catheter with reference to the EnSite coordinate system were recorded.

The MR anatomy scans were segmented using Analyze to isolate the anatomy of interest (right ventricle for patient 1, and left ventricle for patient 2) and an endocardial surface model was generated. The subsequent off-line analysis was different for the two cases:

*Patient 1*: In our previous work [6] we showed how the biplane image acquisition was used to reconstruct the location of the electrical measurement electrodes of the Constellation catheter in the MR derived right heart anatomy. This analysis is now extended. Electrical recordings were made from Constellation electrodes. The recordings were bipolar so that the 64 electrodes produced 32 electrograms with measurement taking place between successive electrodes along each spline. The electrograms were extracted from the measurement system. The position of the 64 electrodes of the Constellation catheter in the MR image space has already been determined. We triangulated this point cloud by using the position of neighboring electrodes to obtain a surface representing the area covered by the basket catheter. Surface to image registration was carried out to correct any error in the alignment of the basket surface and the segmented MR anatomy. Such misalignment may arise due to patient motion and errors in the registration process. The surface to image registration was performed using an iterative closest point algorithm, as proposed by [16]. For each vertex of the basket mesh, the corresponding point in the MR image was found by looking for a boundary point along the normal to the basket surface. The MR image is segmented so the boundary voxels could be easily defined based on the gradient value. The comparison of the gradient direction at this voxel with the vertex normal gives another criterion to confirm if the voxel found is the correct boundary point. Then from all the matched vertex/boundary point pairs we estimated the best rigid body transformation between the Constellation catheter surface and the MR image and this process was iterated until convergence. Once the registration has been refined, the signals from the electrograms were displayed by color coding the basket surface.

*Patient 2*: The EnSite system produced a surface representation of the left ventricle. This was available for further processing as 256 sampled points with corresponding electrograms. Initially, we registered the EnSite system surface to the segmented MR anatomy. A landmark-based registration technique has been reported [19] but we rely on our XMR registration

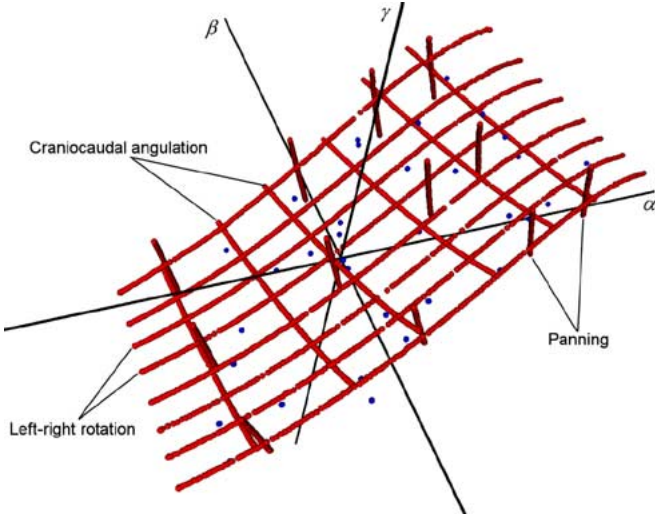


Fig. 4. Coverage of angle space during super global distortion model generation. Each of the red lines corresponds to one of the 26 tracked image intensifier trajectories used to generate the model. The blue points are the 35 test grid images used to validate the model.

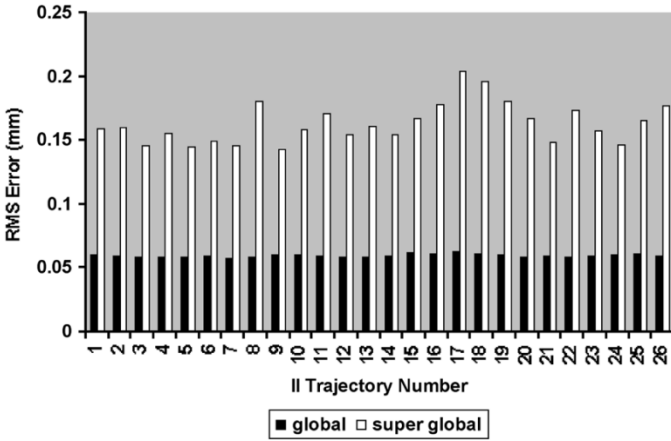


Fig. 5. Mean RMS error for the grid images used to form the distortion model. The mean RMS error is shown for both global and super global correction for the 26 image intensifier trajectories.

technology. We needed to perform a rigid body registration to align the coordinate system of the EnSite surface and the MR volume. Since the location of the distal four electrodes of the roving catheter were measured in the EnSite coordinate system and also determined in the MR coordinate system, it was possible to compute this rigid body transform. Furthermore, the origin of the EnSite coordinate system lies at the center of the balloon catheter. It was possible to compute the location of this point in the MR coordinate system using the registered biplane X-ray views, making a total of five points that were used to find the transformation relating the two coordinate systems. Since the surface given by the EnSite system is an estimation of the end-diastolic endocardium, its shape will not exactly match the left ventricular MR anatomy. Also, there will be errors in the alignment of the EnSite surface and the MR anatomy due to patient motion and errors in the registration process. Therefore, we deformed the EnSite surface to better match the MR image to allow us to proceed with our analysis. This was performed using the deformable surfaces framework [20], where the surface to be deformed evolves under the influence of two ener-

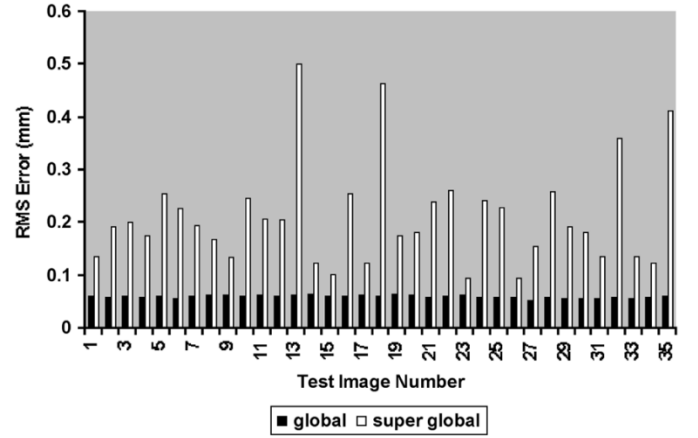


Fig. 6. RMS error for the 35 test grid images used to validate the distortion model. RMS errors are shown for both global and super global correction.

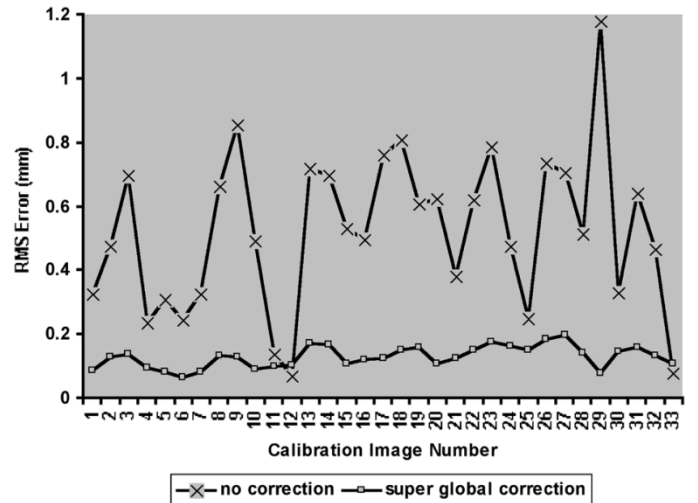


Fig. 7. RMS error for the 33 projection calibration images with and without distortion correction using the super global model.

gies: an external energy aiming to adjust the surface to the image and an internal energy that keeps the surface regular. For each vertex of the surface, the corresponding point in the image is found by looking for a boundary point along the normal of the surface as described earlier. Then a force is applied on the surface proportional to the distance between the vertex and the corresponding boundary point. The dynamics equation is solved using an internal energy smoothing the surface by minimizing the area locally, thus the curvature, as proposed in [21]. Since the location of the poles of the balloon catheter are known with some confidence from the catheter reconstruction process, the corresponding poles of the EnSite surface were constrained to be fixed during the deformation. It was then possible to display the electrograms on the deformed EnSite surface.

### III. RESULTS

#### A. Calibration

1) *X-Ray Image Distortion Correction:* Fig. 4 shows the coverage of angle space during grid imaging. Each of red lines corresponds to one of the 26 tracked image intensifier trajectories. In fact, each of these lines is composed of a series of points corresponding to the 4611 grid images acquired to



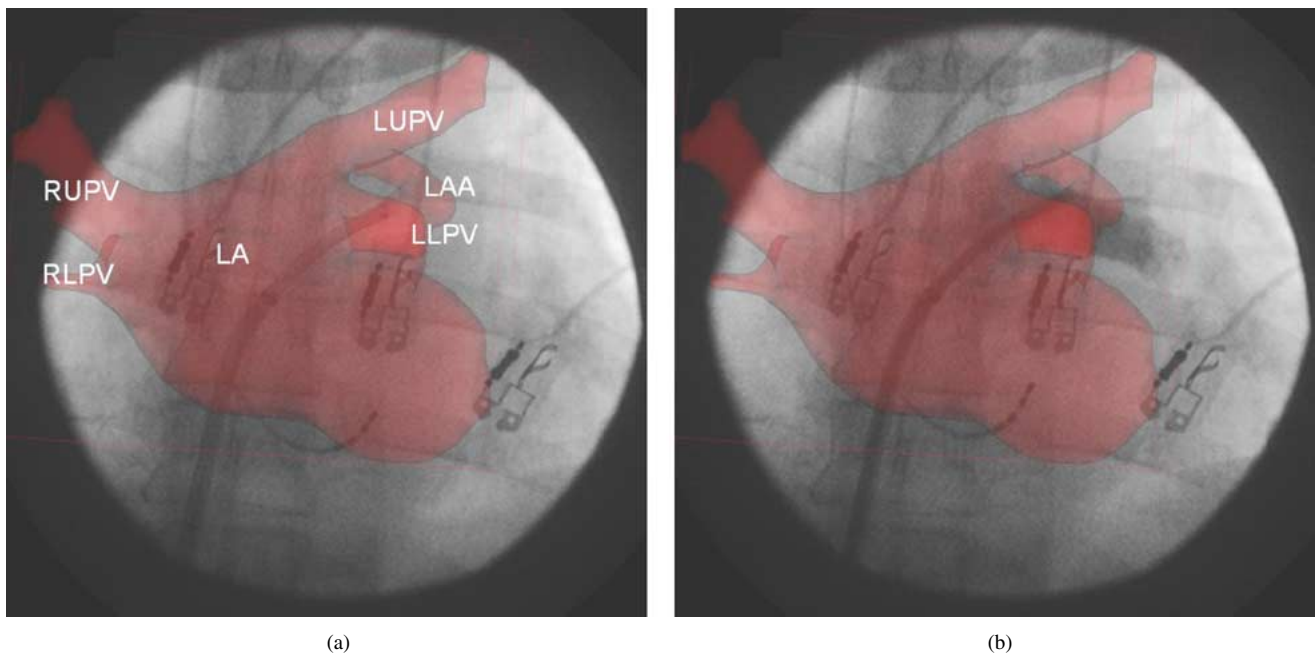


Fig. 8. PV Isolation. Guidance system overlay display showing the delivery catheter in (a) the left lower pulmonary vein and (b) with contrast medium injection. LA = left atrium, LAA = left atrial appendage, PV = pulmonary vein, LU=left upper, LL = left lower, RU = right upper, RL = right lower.

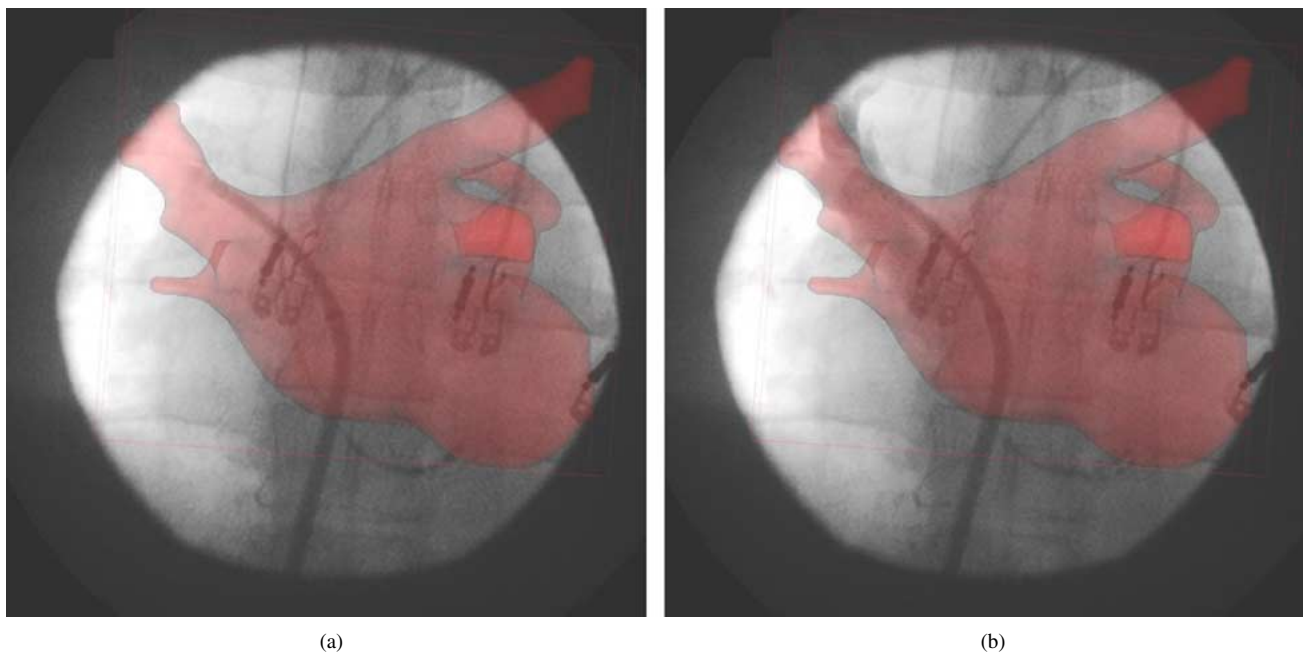


Fig. 9. PV Isolation. Guidance system overlay display showing the delivery catheter in (a) the right upper pulmonary vein and (b) with contrast medium injection.

generate the super global distortion model. The axes are the three Euler angles obtained by extracting the rotational components from the image intensifier tracking matrices. The figure shows that there were eight left-right rotations, six craniocaudal rotations, and 12 panning sequences. The blue points in this image correspond to the 35 test images acquired of the grid to validate the super global model. Fig. 5 shows the RMS residual error for the grid images used to generate the model. The mean RMS error is shown for each image intensifier trajectory for both the global correction (gold standard) and the super global correction. The overall mean global RMS error was 0.060 mm

compared to 0.16 mm for the super global model. Fig. 6 shows the RMS error plot for the 35 test grid images. The mean RMS error for all 35 images for the global correction was 0.060 mm compared to 0.21 mm for the super global model.

2) *X-Ray System Projection Calibration:* The 39 projection calibration images were used to compute an overall projection matrix as described in [6] and the RMS error was computed between the projected location of the calibration object markers and the position found automatically in the X-ray images. The calibration images were distortion corrected using the super global model and the RMS error for the projection calibration



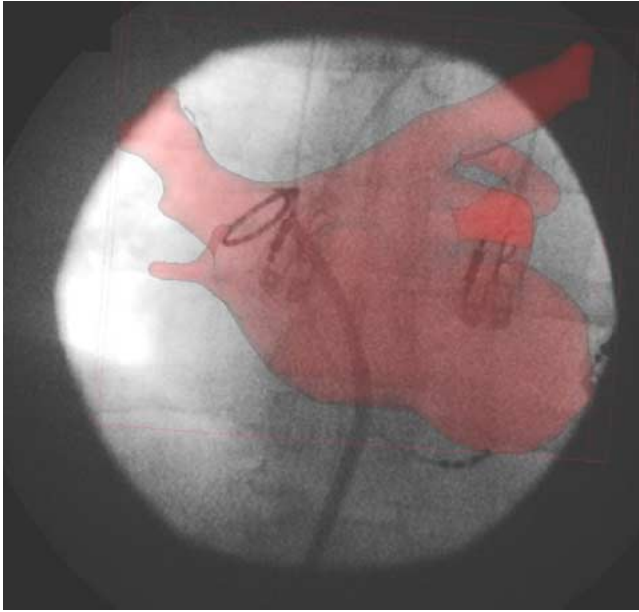


Fig. 10. PV Isolation. Guidance system overlay display showing the helix deployed in the right upper pulmonary vein.

was found to be 1.5 mm ( $n = 398$ ). The RMS error computed using the original distorted images was 1.9 mm. To further investigate the effects of distortion correction on projection calibration, a projection matrix was calculated for each calibration image individually, with and without distortion correction. Since at least six markers need to be identified to compute the projection matrix, this could only be done for 33 out of the 39 calibration images, the others not having a sufficient number of markers. Fig. 7 shows the RMS errors for the 33 images. The RMS error was lower for the corrected images in 31 out of 33 cases. In two cases it was greater for the corrected images but the difference was very marginal. For all 33 images, the mean RMS error with distortion correction was 0.13 and 0.52 mm without correction.

#### B. Clinical Applications

1) *Real-Time Guided Procedures:* Results for one of the real-time guided EPS procedures are presented. These results are taken from a PV isolation procedure during which a helical ablation catheter was guided into three PVs in turn to carry out electrical isolation. Fig. 8(a) shows the guidance system overlay display when the delivery catheter was placed in the left lower PV and Fig. 8(b) shows contrast medium injection into this vein. Fig. 9(a) and (b) shows the catheter in the right upper PV. Fig. 10 shows the helical ablation catheter deployed in the right upper PV during ablation. Finally, Fig. 11 shows the reconstructed location of the helix catheter in all three PVs.

For the aortic stent implantation, the guidance system overlay display was used to continually assess the position of the stent during deployment. Fig. 12(a) shows the delivery catheter and the stent prior to deployment. Fig. 12(b) shows the stent after full deployment. The X-ray view shown was selected using the view selection capability of the guidance system.

2) *Mapping Measured Electrical Activity to MR Derived Anatomy:* For patient 1, Fig. 13(a) shows the basket electrode

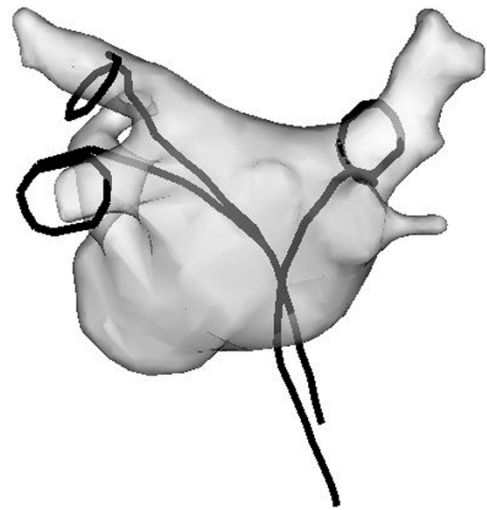


Fig. 11. PV Isolation. The reconstructed location of the helix catheter in the patient anatomy during each ablation.

positions in the MR derived right heart anatomy. Fig. 13(b) and (c) shows the surface mesh generated from the basket electrode points and same mesh transformed rigidly to match the segmented MR anatomy. Fig. 14 is the electrical activity mapped onto the basket mesh showing progression of depolarization during a ventricular ectopic beat.

For patient 2, Fig. 15(a) and (b) shows the original EnSite system surface registered to the segmented MR anatomy and the deformed EnSite surface. Fig. 16 shows the measured electrical depolarization during one cardiac cycle mapped onto the deformed EnSite surface.

#### IV. DISCUSSION AND CONCLUSION

The results for the super global distortion correction model show that we can successfully model and correct the X-ray image distortion for any arbitrary image intensifier orientation. The mean RMS error for the 35 test grid images was 0.21 mm using the super global model compared to 0.060 mm for the gold standard global correction. These results compare well with previously published work [8]–[11]. The incorporation of this distortion model into our guidance system will provide a path to improvement of perspective projection calibration and improve the accuracy of both our combined 2-D and 3-D image representations. We rely on the MR system software for automatically providing MR image distortion correction and from error analysis during the calibration stage we can conclude that the residual error due to distortion in the calibration MR scan is very small compared to the other errors that contribute to the overall registration accuracy.

In our previous validation study we showed that the errors in our registration algorithm were 2.4–4.2 mm for the combined 2-D image representation and 4.6–5.1 mm for the combined 3-D image representation for static phantoms. These errors can be put into anatomical context if we consider that the diameter of an adult human pulmonary vein is approximately 15 mm. In Section III-A2 the RMS error for overall projection calibration was found to be 1.9 mm. This contributes the largest error to the

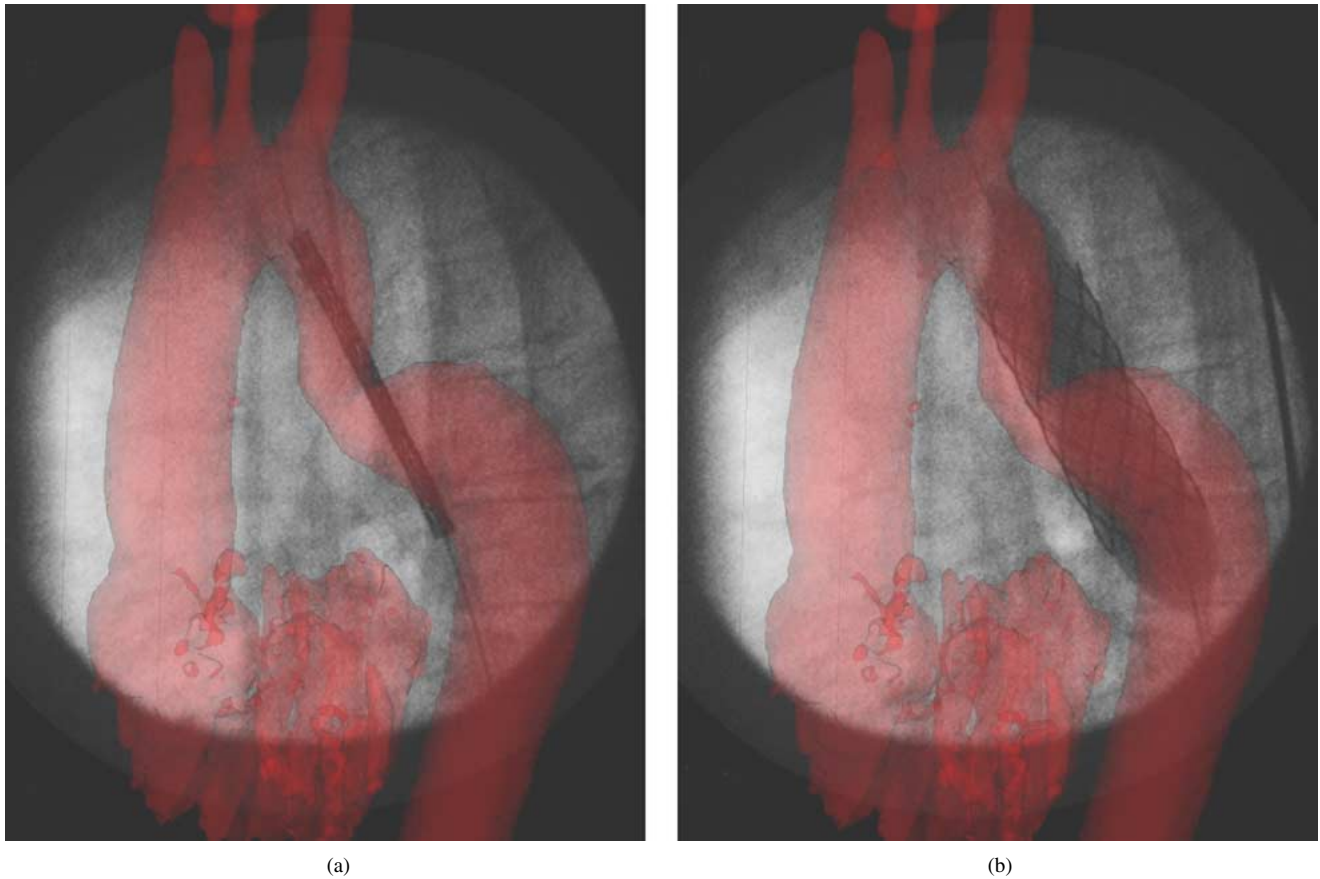


Fig. 12. Aortic stent implantation. Guidance system overlay showing stent in position (a) prior to deployment and (b) the stent fully deployed.

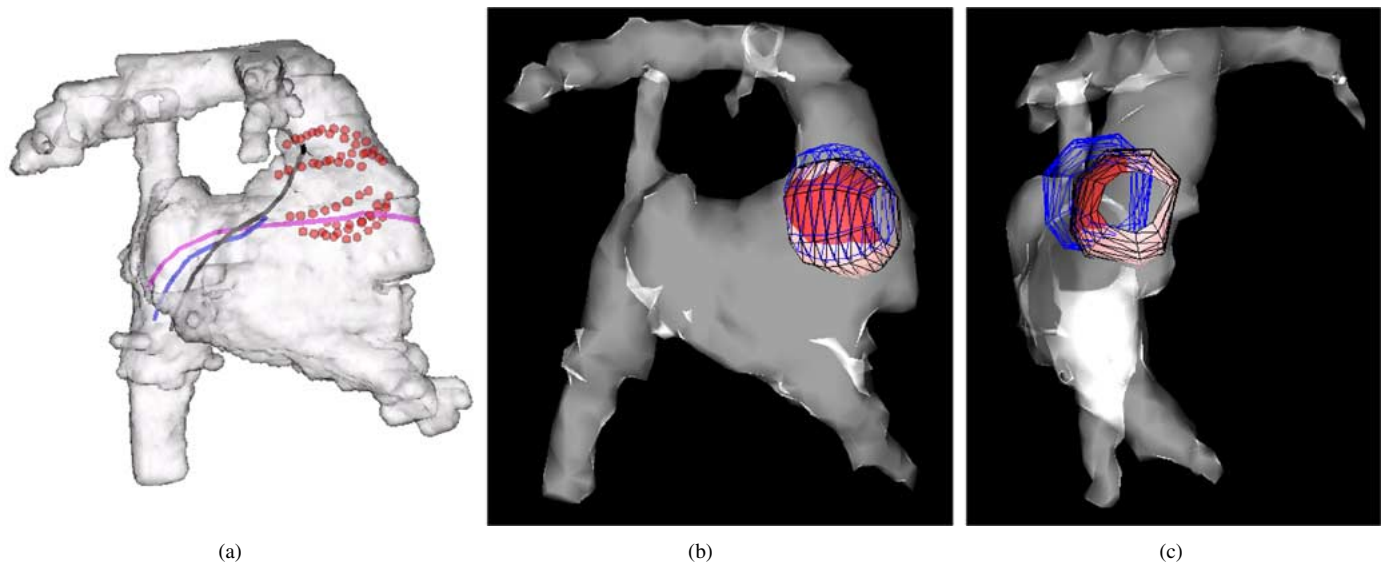


Fig. 13. EPS using basket catheter. (a) Path of the catheters and the electrode positions are displayed in the segmented MR anatomy of the right heart. (b) and (c) Position of the mesh generated from the Constellation catheter electrode points is shown before (blue) and after (red) rigid body transformation.

overall registration accuracy. The use of the super global distortion model to correct the geometric distortion in the projection calibration images resulted in an improvement of error from 1.9 mm to 1.5 mm. The results from single image projection calibration with distortion correction give a mean RMS error of 0.13 mm. Since the X-ray system c-arm can be moved freely during a procedure it is not possible to use single image projec-

tion calibration and the calibration must be derived from multiple X-ray views. The discrepancy of more than 1 mm between single and multiple projection calibration can be attributed to the contribution of gantry sag. In on going work we are using a scheme similar to our method of super global distortion correction to model the perspective projection parameters as a function of image intensifier orientation.

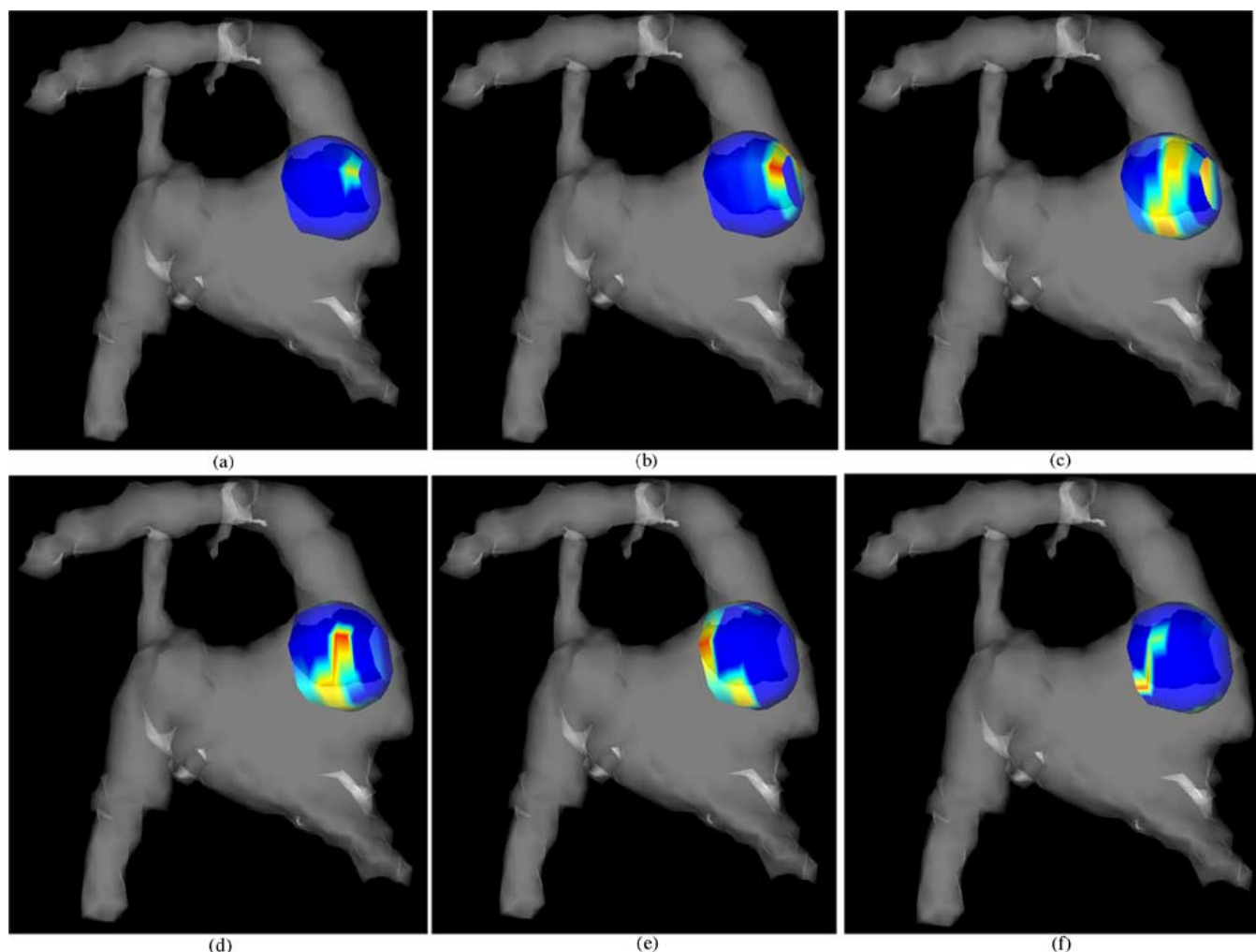


Fig. 14. EPS using basket catheter. The progression of depolarization during an ectopic beat arising from the right ventricular outflow tract. The ectopic focus can be seen in the first frame.

We have applied our real-time guidance system to 10 EPS cases and one aortic stent placement case. The results show two exemplar cases. During the EPS cases, the real-time overlay display provided a roadmap for positioning ablation catheters, reducing the requirement for repeated contrast medium injection. For the PV ablation cases, the roadmap was used to prevent inadvertent catheterization of PV branches and facilitated delivery catheter repositioning from one PV to the next. In three separate instances it was seen from the roadmap that the same PV had been inadvertently recatheterized. Also, the 3-D reconstruction of the helical ablation catheter was used to assess catheter lie prior to delivery of the ablation current. For the aortic stent placement, the overlay display was used in the positioning of the stent delivery catheter across the aortic coarctation. The guidance system was also used to carry out X-ray view selection without administration of X-ray dose.

For the ventricular EPS cases we have demonstrated how our off-line analysis was used to display the measured ventricular electrical activity in the patient specific cardiac anatomy. This type of display will be of great benefit during EPS cases and in future work we aim to automate the steps required to make this possible. Currently we have used the integrated electrical and anatomical data along with registered myocardial motion de-

rived from the tagged MR imaging [22], [23] to explore electro-mechanical models of the myocardium [24], [25].

In conclusion, we have described an XMR guidance system that provides real-time integration of recently acquired MR images and live X-ray images, and enables subsequent integration of anatomy, motion and catheter-based electrophysiological recordings. This substantially extends our previous work on off-line combination of X-ray and MR images in the following ways. First, we have updated our registration software so that combined MR and X-ray images can be displayed in real-time to provide guidance during cardiovascular interventions. Second, we have used purposely built optical trackers and calibration object resulting in a single robust calibration stage with the ability to check and update calibration efficiently prior to each patient procedure. Third, we have implemented an X-ray distortion correction model that allows for geometric distortion correction for arbitrary image intensifier orientations. This will allow for improved X-ray perspective calibration. Although this will improve our overall registration accuracy, the ability to deal with patient motion is the limiting factor for our technique. Therefore, we will focus on strategies to correct for this in future work. Finally, we have extended our previous off-line analysis to allow visualization of cardiac electrical ac-



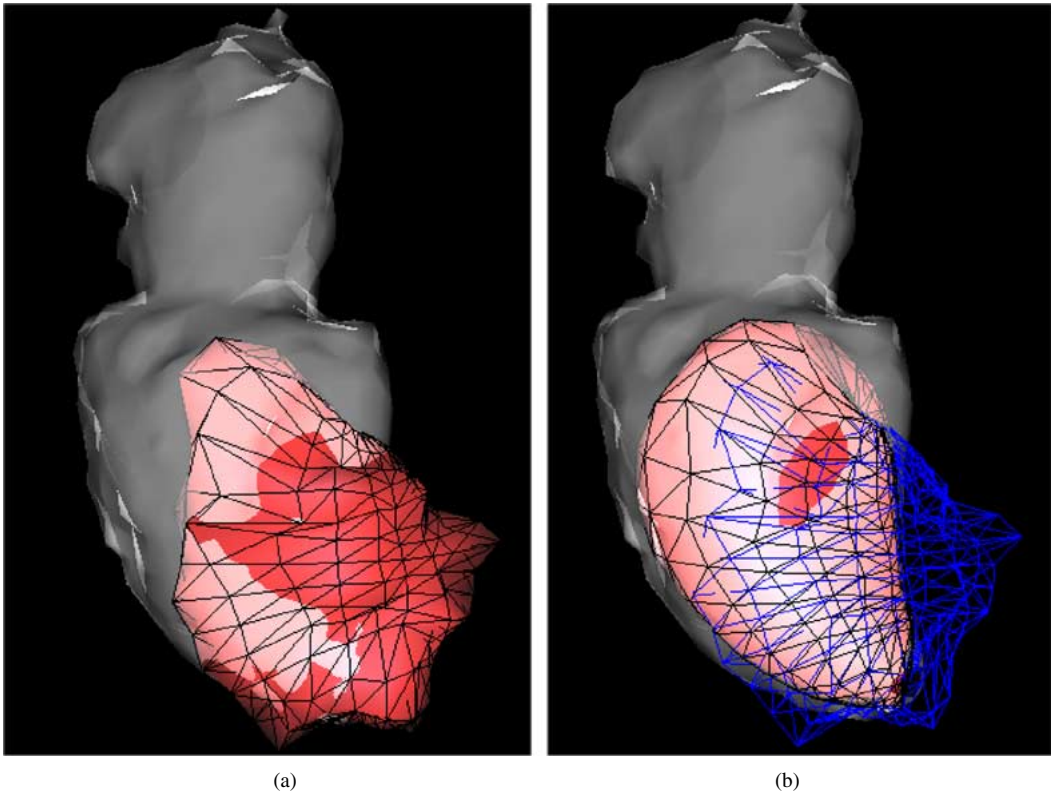


Fig. 15. EPS using EnSite system. (a) The EnSite surface is shown registered to the segmented MR anatomy. (b) Deformed EnSite surface (red) is shown along with the initial registered surface (blue).

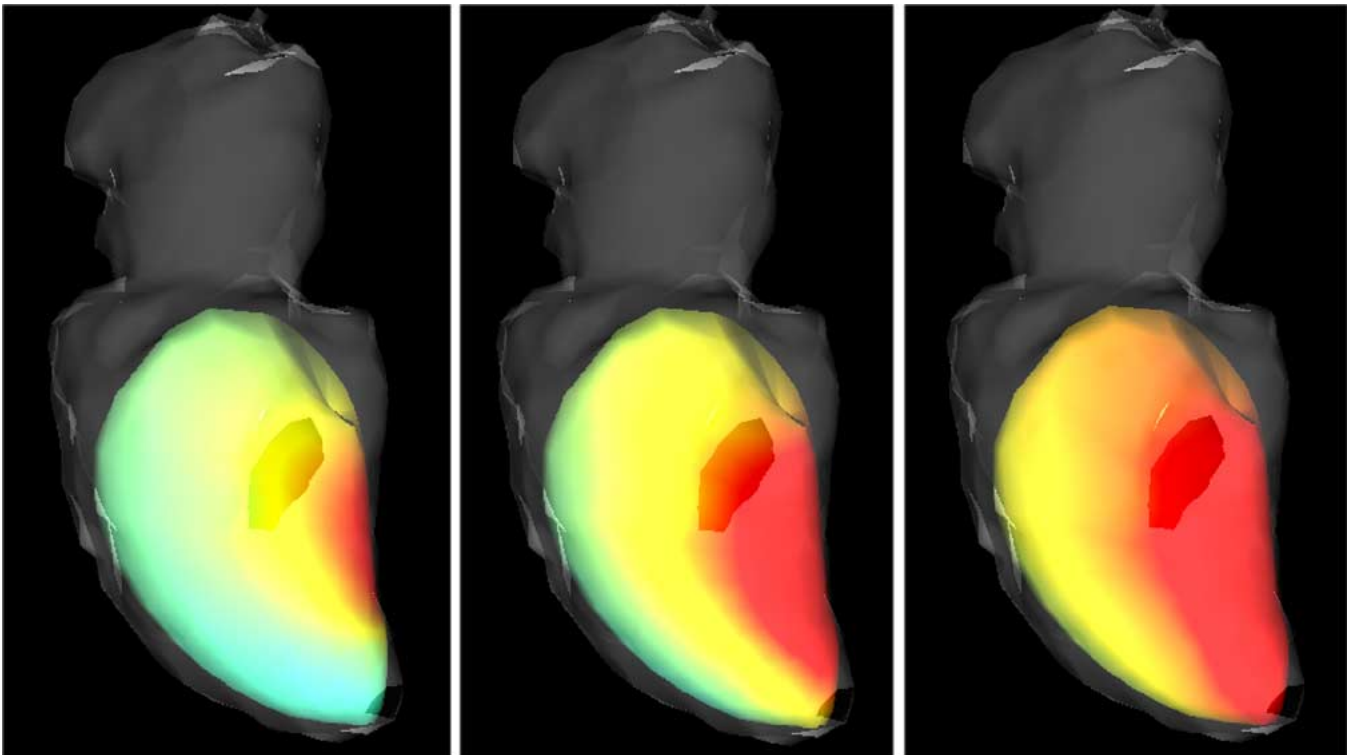


Fig. 16. EPS using EnSite system. The measured electrical depolarization for three phases of the cardiac cycle.

tivity in patient specific anatomy using two types of electrical mapping catheters. The cardiologists that have used the guidance system suggest that real-time XMR guidance could have substantial value in difficult interventional and electrophysiological procedures, potentially reducing procedure time and delivered radiation dose.

## ACKNOWLEDGMENT

The authors acknowledge A. Black for the construction of the optical trackers and the calibration object. The authors acknowledge the contributions of D. Elliott and Endocardial Solutions Inc. They would also like to acknowledge the use of the MIPS software from the Epidaure project, INRIA, France.

## REFERENCES

- [1] J. J. V. Vaals, G. Adam, and R. W. Günther, "Initial experience of combining a 1.5 T MR system with X-ray fluoroscopy for interventional MR procedures," in *Proc. Radiological Soc. North America, 81th Scientific Assembly and Annual Meeting, Abstract 564*, in *Radiology*, vol. 197, 1995, pp. 220–224.
- [2] J. J. V. Vaals, "Interventional MR on a hybrid high-field system," in *Interventional Magnetic Resonance Imaging*, J. Debatin and G. Adam, Eds. New York: Springer, 1997, ch. 3, pp. 17–30. ISBN 3-540-62587-9.
- [3] A. H. Mahnken, K. Chalabi, F. Jalali, R. W. Gunther, and A. Buecker, "Magnetic resonance-guided placement of aortic stents grafts: Feasibility with real-time magnetic resonance fluoroscopy," in *J. Vasc. Interv. Radiol.*, 2004, vol. 15, pp. 189–195.
- [4] S. Schalla, M. Saeed, C. B. Higgins, A. Martin, O. Weber, and P. Moore, "Magnetic resonance-guided cardiac catheterization in a swine model of atrial septal defect," *Circulation*, vol. 108, no. 15, pp. 1865–1870, 2003.
- [5] R. Razavi, D. L. Hill, S. F. Keevil, M. E. Miquel, V. Muthurangu, S. Hegde, K. Rhode, M. Barnett, J. V. Vaals, D. J. Hawkes, and E. Baker, "Cardiac catheterization guided by MRI in children and adults with congenital heart disease," *Lancet*, vol. 362, no. 9399, pp. 1877–1882, 2003.
- [6] K. S. Rhode, D. L. Hill, P. J. Edwards, J. Hipwell, D. Rueckert, G. Sanchez-Ortiz, S. Hegde, V. Rahunathan, and R. Razavi, "Registration and tracking to integrate X-ray and MR images in an XMR facility," *IEEE Trans. Med. Imag.*, vol. 22, no. 11, pp. 1369–1378, Nov. 2003.
- [7] K. S. Rhode, D. L. G. Hill, P. J. Edwards, J. Hipwell, D. Rueckert, G. Sanchez-Ortiz, S. Hegde, V. Rahunathan, and R. Razavi, "Application of XMR 2D-3D registration to cardiac interventional guidance," in *Proc. MICCAI*, vol. 2878, 2003, pp. 295–302.
- [8] P. Haaker, E. Klotz, R. Koppe, and R. Linde, "Real-time distortion correction of digital X-ray II/TV-systems: An application example for digital flashing tomosynthesis (DFTS)," *Int. J. Cardiol. Imag.*, vol. 6, no. 1, pp. 39–45, 1990–1991.
- [9] R. Fahrig, M. Moreau, and D. W. Holdsworth, "Three-dimensional computed tomographic reconstruction using a C-arm mounted XR2: Correction of image intensifier distortion correction," *Med. Phys.*, vol. 24, pp. 1097–1106, 1997.
- [10] R. Liu, S. Rudin, and D. Bednarek, "Super-global distortion correction for a rotational C-arm X-ray image intensifier," *Med. Phys.*, vol. 26, no. 9, pp. 1802–1810, 1999.
- [11] C. Canero, F. Vilarino, J. Mauri, and P. Radeva P, "Predictive (un)distortion model and 3-D reconstruction by biplane snakes," *IEEE Trans. Med. Imag.*, vol. 21, no. 9, pp. 1188–1201, Sep. 2002.
- [12] D. J. Hawkes, A. C. F. Colchester, and C. Mol, "The accurate 3D reconstruction of the geometric configuration of vascular trees from X-ray recordings," in *Physics and Engineering of Medical Imaging*, R. Guzzardi, Ed. The Hague, The Netherlands: Martinus Nijhoff, 1985.
- [13] M. Eldar, D. G. Ohad, J. J. Goldberger, Z. Rotstein, S. Hsu, D. K. Swanson, and A. J. Greenspon, "Transcutaneous multielectrode basket catheter for endocardial mapping and ablation of ventricular tachycardia in the pig," *Circulation*, vol. 96, no. 7, pp. 2430–2437, 1997.
- [14] C. Schmitt, B. Zrenner, M. Schneider, M. Karch, G. Ndrepepa, I. Deisenhofer, S. Weyerbrock, J. Schreieck, and A. Schomig, "Clinical experience with a novel multielectrode basket catheter in right atrial tachycardias," *Circulation*, vol. 99, no. 18, pp. 2414–2422, 1999.
- [15] I. H. D. Boer, F. B. Sachse, and O. Doessel, "A model-based approach for localization of basket catheters for endocardial mapping," in *Proc. CARS*, 2000, p. 1004.
- [16] J. Montagnat and H. Delingette, "Globally constrained deformable models for 3D object reconstruction," *Signal Process.*, vol. 71, no. 2, pp. 173–186, 1998.
- [17] K. Okishige, M. Kawabata, S. Umayahara, K. Yamashiro, M. Gotoh, M. Isobe, and S. A. Strickberger, "Radiofrequency catheter ablation of various kinds of arrhythmias guided by virtual electrograms using a noncontact, computerized mapping system," *Circ. J.*, vol. 67, no. 5, pp. 455–460, 2003.
- [18] P. D. Lambiase, A. Rinaldi, J. Hauck, M. Mobb, D. Elliott, S. Mohammad, J. S. Gill, and C. A. Bucknall, "Non-contact left ventricular endocardial mapping in cardiac resynchronization therapy," *Heart*, vol. 90, no. 1, pp. 44–51, 2004.
- [19] Z. J. Malchano, R. C. Chan, G. Holmvang, E. J. Schmidt, A. D'Avila, T. J. Brady, J. N. Ruskin, and V. Y. Reddy, "Registration strategies for alignment of cardiac MR data with 3D electrophysiology maps," presented at the 11th Int. Soc. Mag. Reson. Med., Toronto, ON, Canada, July 10–16, 2003.
- [20] J. Montagnat and H. Delingette, "A review of deformable surfaces: Topology, geometry and deformation," *Image Vis. Computing*, vol. 19, no. 14, pp. 1023–1040, 2001.
- [21] M. Desbrun, M. Meyer, P. Schröder, and A. Barr, "Implicit fairing of arbitrary meshes using diffusion and curvature flow," in *Proc. Int. Conf. Computer Graphics and Interactive Techniques (ACM Siggraph'99)*, 1999, pp. 317–324.
- [22] R. Chandrashekar, R. H. Mohiaddin, and D. Rueckert, "Analysis of myocardial motion in tagged MR images using nonrigid image registration," *Proc. SPIE, Medical Imaging*, vol. 4684, pp. 1168–1179, 2002.
- [23] G. Sanchez-Ortiz, R. Chandrashekar, K. S. Rhode, R. Razavi, D. L. G. Hill, and D. Rueckert, "Detecting regional changes in myocardial contraction patterns using MRI," *Proc. SPIE, Medical Imaging*, vol. 269, pp. 710–721, 2004.
- [24] K. S. Rhode, M. Sermesant, S. Hegde, G. Sanchez-Ortiz, D. Rueckert, R. Razavi, and D. L. G. Hill, "XMR guided cardiac electrophysiology study and radio frequency ablation," *Proc. SPIE, Medical Imaging*, vol. 5369, pp. 10–21, 2004.
- [25] M. Sermesant, K. Rhode, A. Anjorin, S. Hegde, G. I. Sanchez-Ortiz, D. Rueckert, P. Lambiase, C. A. Bucknall, D. L. Hill, and R. Razavi, "Simulation of the electromechanical activity of the heart using XMR interventional imaging," in *Proc. MICCAI*, vol. 3217, 2004, pp. 786–794.